Evolution of water budget and precipitation efficiency of mesoscale convective systems over the South China Sea

Yao-Chu Wu, Ming-Jen Yang [*], and Po-Hsiung Lin

Department of Atmospheric Sciences, National Taiwan University, Taipei City, Taiwan

ABSTRACT

In this study, the evolution of precipitation efficiency (PE) and water budget of mesoscale convective systems (MCSs), which produced heavy rainfall over the South China Sea and southern Taiwan on 25 - 28 August 2015, are investigated using satellite observations and model simulations. The MCS is embedded within the southwesterly monsoon flow from Indo China with abundant moisture. The evolution of PE and water budget is first examined in a quasi-Lagrangian framework following the movement of targeted MCS, and is confirmed in an Eulerian framework over the broad-scale area enclosing the MCS. The sensitivity of water budget and moisture fluxes to low-level moisture amount and horizontal wind speed is investigated. Water budget in the quasi-Lagrangian framework shows that if the low-level large-scale moisture is increased (decreased) by 10%, the total condensation and deposition will be increased (decreased) by 10% (30 - 40%); moisture flux convergence will be significantly enhanced within the MCS to generate more precipitation, and evaporation will be more pronounced over the region of weak convection. Similar results are found in an Eulerian framework. For the strong convective cells (radar reflectivity of greater than 35 dBZ) within the MCS, the calculated large-scale PE is 20 - 25% and the microphysical PE is 35 - 40%. The surface precipitation is highly sensitive to the large-scale moisture change, and less sensitive to wind-speed change. In particular, 10% decrease of low-level (below 700 hPa) relative humidity results in 10 - 20% decrease of moisture flux and 10 - 40% reduction of surface precipitation.

1. INTRODUCTION

The southwesterly monsoon flow accompanied by Mei-Yu fronts and tropical cyclones takes place near Taiwan and South China Sea (SCS) during the summer season. Mesoscale convective systems (MCSs) embedded in the southwesterly flow can cause heavy rainfalls on the windward side of Central Mountain Range (CMR; Yeh and Chen 1998, 2002; Teng et al. 2000; Chen and Chen 2003). With abundant moisture transport and strong wind at low levels for a long distance (1000 km or longer), the southwesterly monsoon flow in East Asia may be considered as one type of the atmospheric rivers (ARs; Kamae et al. 2017). Du and Chen (2019) and Tu et al. (2019) discussed the relationship between southwesterly monsoon flow, low-level jet, and rainfall over the South China Sea.

AR is a narrow filament region that transports massive water vapor from the Tropics to midlatitudes (Zhu and Newell 1998). ARs often appear within the warm conveyor belt of extratropical cyclones with high water-vapor content, low-level jets and moist-neutral stratification in the vertical (Ralph et al. 2004, 2005; Gimeno et al. 2014). Previous studies focused on the AR events over the west coast of North America (e.g., Neiman et al. 2008a, b; Dettinger et al. 2011; Mueller et al. 2017), Europe (e.g., Stohl et al. 2008; Lavers et al. 2012; Ramos et al. 2015), and Africa (Brands et al. 2017). The main sources of water vapor in ARs are associated with low-level water vapor flux convergence in pre-frontal areas and the poleward transport from tropical regions (Bao et al. 2006). Taiwan Island is located in the middle of the ARs corridor over East Asia. Furthermore, a better prediction of the occurrence and maintenance of ARs lays the fundamental for a better forecast of weather, climate, and hydrological cycle. Thus, it is important to examine the impact of water

* Corresponding author
  E-mail: mingjen@as.ntu.edu.tw

vapor transport within the AR to Taiwan.

Through high-resolution simulations and water budget diagnostics, we can better understand the precipitation mechanisms within tropical cyclones (TCs). Braun (2006) found that the majority of condensation takes place within the convective hot towers in the TC eyewall, while vapor deposition and aggregation occur in the outer region of TC to enhance the stratiform precipitation. Yang et al. (2011) indicated that the precipitation was enhanced when Typhoon Nari (2001) made landfall on Taiwan terrain, resulting from the enhanced moisture convergence through the intensification of low-level inflow and the increased condensation and deposition. Huang et al. (2014) followed the motion of several convective cells within the rainbands of Typhoon Morakot (2009) in a quasi-Lagrangian framework, and they found that the enhanced convective updrafts condensed more water vapor on the CMR's windward side, and the reverse was true on the lee side. Xu et al. (2017) used particle trajectories to discuss the rainfall budget and raindrop microphysical budget of Typhoon Fitow (2013) in the Lagrangian perspective, and they found that the hydrometeor gain/divergence occurred near the rainfall centers of TC Fitow and transported hydrometeors to produce tremendous rainfall. Similar mechanisms may also occur within the MCSs.

Precipitation efficiency (PE) is an essential parameter to examine precipitation mechanism of convective system. In general circulation models, cumulus parameterizations use this parameter to convert portions of large-scale water vapor convergence into the subgrid-scale precipitation. As computational computers increase with time, numerical weather prediction (NWP) models and cloud-resolving models are able to represent precipitation by more complicated cloud microphysics parameterizations. There are two ways to calculate the PE. One is the large-scale precipitation efficiency (LSPE), which is defined as the ratio of precipitation over three-dimensional water vapor convergence and surface evaporation (Kuo 1965, 1974). This LSPE is widely used in observation studies because water-vapor convergence and surface evaporation are easily obtained from sounding or field campaign data. The other is the cloud-microphysics precipitation efficiency (CMPE), which is defined as the ratio of precipitation over condensation (Weisman and Klemp 1982; Lipps and Hemler 1986). Li et al. (2002) found that the CMPE and LSPE would exceed 100% or become negative, which were physically unreasonable. Sui et al. (2007) proposed refinement of the PEs, the LSPE2 and CMPE2, to prevent their values from exceeding 100% or negative such that the PEs are more physically reasonable.

Since horizontal water vapor flux is composed by both water vapor (or relative humidity) and horizontal wind, it is worth to examine the sensitivity of water-vapor transport to low-level relative humidity and wind speed. Schumacher (2015) conducted an idealized MCS simulation with 0.3 - 1% changes of integrated water vapor at near-surface stable layer. He found that precipitation is more sensitive to environmental relative humidity with the point maxima changed up to 29% for the accumulated rainfall. Morales et al. (2018) performed a 30% horizontal wind-speed reduction sensitivity experiment throughout the entire vertical profile in sounding data, and found that wind-speed reduction experiment has significant effect on precipitation but the microphysics parameters have similar response to the control run.

The objective of this study is to investigate the water-vapor transport by MCSs embedded within the southwesterly monsoon flow (or AR) over the East Asia. The following scientific questions will be addressed in this study:

(1) How does water vapor transport along the AR change with water-vapor increasing (or decreasing) or wind-speed acceleration (or deceleration) at lower levels?

(2) How does the precipitation efficiency of the MCS evolve along the AR?

(3) How does the condensation ratio, deposition ratio, and raindrop evaporation ratio within the MCS change from ocean to land?

The reminder of the paper is organized as follows. Section 2 describes the model configuration and sensitivity experiments design. In section 3, the simulated AR pattern and precipitation distribution are verified and discussed. The large-scale water vapor transports of the control and sensitivity experiments are investigated and compared. In section 4, the changes of water budget, PE, and microphysics ratios of the targeted MCS are analyzed. Concluding remarks are given in section 5.

2. EXPERIMENTS DESIGN

The Advanced Research Weather Research and Forecasting model (ARW version 3.9; Skamarock et al. 2008) is used to simulate the AR event from 0000 UTC 25 August to 1800 UTC 28 August 2015, with a forecast period of 90 hrs. Triply-nested domains (with horizontal grid sizes of 27-, 9-, and 3-km) are shown in Fig. 1. The ERA-Interim reanalysis data (Dee et al. 2011) with the latitude-longitude resolution of 0.75 degree, which is produced by the European Centre for Medium-Range Weather Forecasts (ECMWF), is used as the initial and lateral boundary conditions for the WRF model. Lateral boundary conditions of the outmost grid are updated every 6 hrs. Two-way feedback between inner and outer domain is taken into account. Fifty-five eta levels are used in the vertical with higher resolution in the planetary boundary layer. The model top is at 30 hPa.

The physical parameterization schemes used in the model include the Dudhia (1989) shortwave radiation parameterization, Rapid Radiative Transfer Model (RRTM) longwave radiation parameterization (Mlawer et al. 1997), Yonsei University (YSU) planetary boundary layer parameterization (Hong et al. 2006), Grell-Devenyi ensemble
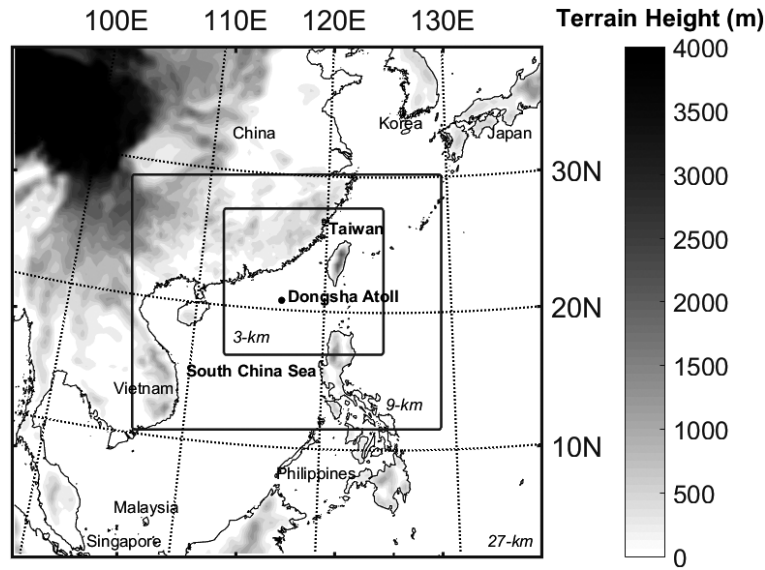
Fig. 1. WRF nested domains with terrain-height shading. The black dot (at 116.7°E, 20.7°N) is Dongsha Atoll (Island).

cumulus parameterization (Grell and Dévényi 2002), and Morrison two-moment microphysics parameterization (Morrison and Gettelman 2008; Morrison et al. 2009). Note that the innermost (3-km) and intermediate (9-km) domains do not use the cumulus parameterization, assuming that convection can be explicitly resolved by the model grids. The sea surface temperature stays fixed in time throughout the simulation.

In addition to the control simulation (CTL), four numerical experiments are performed to examine the sensitivity of water-vapor transport to the variations of low-level relative humidity and horizontal wind speed. The experiment with relative humidity wetter (or drier) by 10% from the CTL at low levels (surface to 700 hPa) is called as W10 (or D10). Note that when the relative humidity exceeds 100%, it remains saturation to prevent from unrealistic super-saturation condition in large-scale moisture analysis. The experiment with wind speed faster (or slower) by 10% from the CTL at low levels (surface to 700 hPa) is named as F10 (or S10); as the low-level wind speed is changed, the corresponding mass adjustment is also performed by calculating the balanced mass change through the potential vorticity inversion (Davis 1992). The adjustments are conducted in both the initial and boundary conditions for the WRF sensitivity simulations.

3. LARGE SCALE WATER VAPOR TRANSPORT

3.1 Model Verification

In order to quantify the water-vapor transport along the AR, we used the integrated water vapor (IWV), integrated mass transport (IMT), and integrated water-vapor transport (IVT) which are defined as follows:

$$IWV = \frac{1}{g} \int_{sfc}^{200\ hPa} q_v\, dp \tag{1}$$

$$IMT = \frac{1}{g} \int_{sfc}^{200\ hPa} \vec{U}\, dp \tag{2}$$

$$IVT = \frac{1}{g} \int_{sfc}^{200\ hPa} q_v \vec{U}\, dp \tag{3}$$

where g is gravitational acceleration, q_v is water vapor mixing ratio, $\vec{U}$ is the total horizontal wind vector, and p is the pressure level. The IWV indicates the total amount of the water vapor (or precipitable water) available in the atmospheric column. The IMT is the vertical integration of horizontal wind that reveals the magnitude and direction of air mass transport. The IVT is the summation of water-vapor flux at each vertical level, indicating the magnitude and direction of the integrated moisture transport.

Figures 2 and 3 illustrate the horizontal distribution of the IWV and IVT from the ERA-Interim analyses (0.125-degree resolution) and 27-km CTL simulation, respectively. The slantwise rectangular box in northeast-southwest orientation, which is 2025-km long and 945-km wide, covers the major convection features along the AR. Both the IWV and IVT are two main indicators to identify the ARs (Zhu and Newell 1998; Ralph et al. 2004; Smith et al. 2010; Dettinger et al. 2011; Gimeno et al. 2014). Note that the CTL simulation has greater magnitude of IWV and IVT than the analyses, probably due to stronger convective systems in the simulation.

Figures 2a and d show that the IWV was concentrated over the SCS at 0000 UTC 26 August 2015. In Figs. 2b and e,
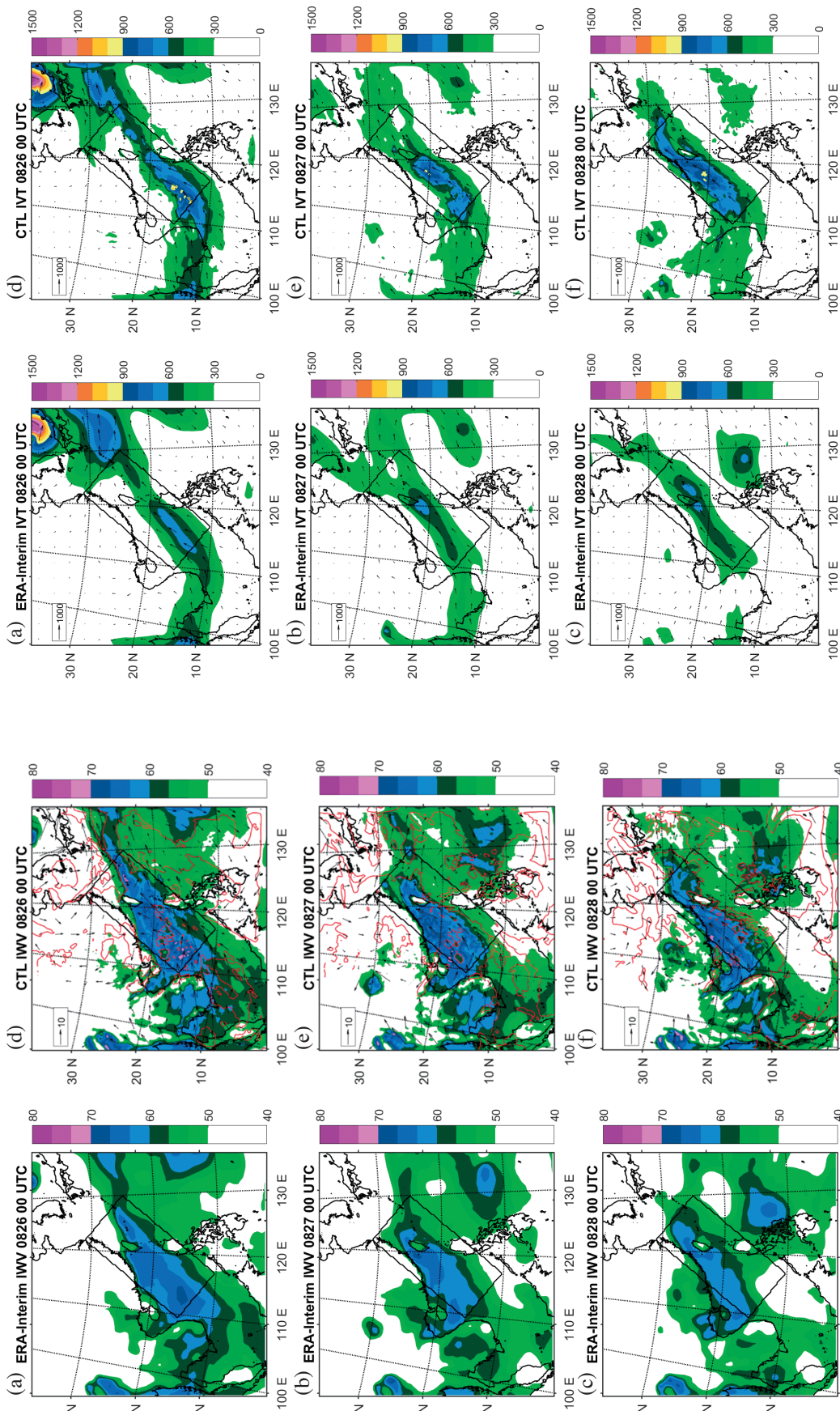
Fig. 2. The horizontal distribution of integrated water vapor (IWV; unit: mm) diagnosed from (a) - (c) ECMWF ERA-Interim reanalysis dataset on the 0.125° grid and from (d) - (f) 27-km CTL simulation at (a) (d) 0000 UTC 26 August; (b) (e) 0000 UTC 27 August; (c) (f) 0000 UTC 28 August 2015. The slantwise rectangular box along the atmospheric river is also indicated. The red contours indicate the relative-humidity contours of 70% at 850 hPa and the vectors are horizontal wind vectors at 850 hPa.
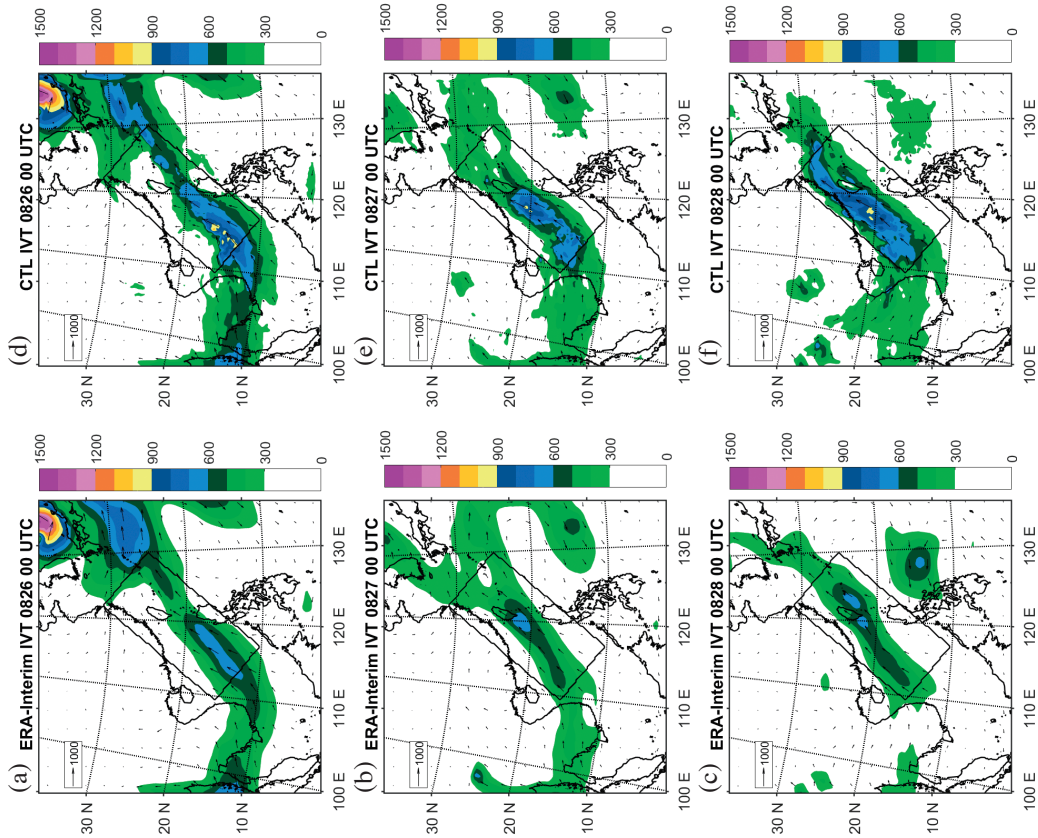
Fig. 3. Similar to Fig. 2 but for integrated water-vapor transport (IVT; unit: kg m⁻¹ s⁻¹).

the IWV shifted northward at 0000 UTC 27 August. The local maximum of IWV appears in the southwest of Taiwan. The abundant moisture leads to the torrential rainfall in southwestern Taiwan. Figures 2c and f show that the area of IWV greater than 60 mm occurs in the Taiwan Strait at 0000 UTC 28 August, indicating that the AR continued to move northward. Some amount of water vapor is able to transport to the east of Ryukyu Islands.

As shown in Figs. 3a and d, the IVT is located to the west of Luzon Island with a narrower structure than the IWV. The IVT reveals that water vapor originates from the Bay of Bengal and passes through the Indochina, and the IVT was further enhanced over the SCS, suggesting that the warm sea surface temperature supplies the moisture flux from the underlying ocean to the AR. The maxima of IVT appeared over the central region of the SCS. On the downstream side, the AR passes through Luzon Strait to transport the moisture to the east of Japan. Figures 3b and e illustrate that the IVT shifted northward and the maxima appeared to the southwest of Taiwan. It is evident that the IVT was enhanced on the windward (western) side of CMR and weakened on the lee (eastern) side, implying that more precipitation was produced on the windward side due to terrain blocking. Less moisture penetrated into the midlatitude. Figures 3c and f display the transport of water vapor into the midlatitude through the east of Taiwan and Taiwan Strait, respectively. The difference between simulation and observation may be caused by the position errors of simulated MCSs. It is found that the location of maximum water-vapor transport is associated with the axis of strongest horizontal wind (cf. Fig. 2).

The global precipitation data from the Climate Prediction Center morphing (CMORPH) technique (the description of the dataset can be found at https://rda.ucar.edu/datasets/ds502.3/) are used to verify the precipitation simulation in the CTL. The CMORPH algorithm combines low-orbiter satellite microwave and geostationary satellite infrared observation data at 0.25-degree horizontal grid size and 3-hr time interval. Figure 4 shows the comparison of accumulated precipitation between CMORPH analysis (Fig. 4a) and CTL simulation (Fig. 4b) from 0900 UTC to 1200 UTC 27 August 2015. The CTL simulation captures the rainfall pattern associated with the AR from the SCS to Taiwan reasonably well. The CTL run produces a rainfall distribution similar to the CMORPH analysis, although the simulated rainfall is overestimated over the SCS (upstream of Taiwan) but underestimated near Taiwan and Japan. Figure 5 shows the comparison between observed and simulated sounding at Dongsha Atoll at 27 August, and it clearly illustrates that the observed sounding at Dongsha is well captured by the CTL simulation.

3.2 Sensitivity Experiments

Figure 6 displays the horizontal distribution of simu-lated IWV in four sensitivity experiments at 0000 UTC 27 August 2015. The IWV in W10 (D10) run has higher and wider (lower and narrower) zones of high moisture content with the IWV > 60 mm than the CTL run. On the other hand, the faster (or slower) wind-speed run F10 (S10) does not change the IWV evidently (Figs. 6c and d). It is worth noticing that the high-moisture area (IWV > 60 mm) is able to expand northward in W10 and F10 experiments.

Figure 7 illustrates the horizontal distribution of the simulated IVT in four sensitivity experiments at 0000 UTC 27 August 2015. Figures 7a and b show that the IVTs in W10 and D10 experiments have significant changes due to water-vapor variations below 700 hPa. In the W10 simulation, the simulated IVT can carry more moisture within the AR to extend northward (Fig. 7a). On the opposite, the simulated IVT is weaker and narrower when low-level water vapor is reduced in D10 run (Fig. 7b). Unlike the IWV, the IVT is slightly stronger (weaker) in F10 (S10) experiment than the CTL, because the IVT is a parameter closely related to the horizontal wind vector (Figs. 7c and d).

To quantify the influence of water-vapor and wind-speed variations at low levels, we calculate the area-averaged IWV, IMT, and IVT along the slantwise rectangular box within the AR. The slantwise areas in the CTL and sensitivity experiments are shown in Figs. 2 and 3. Figures 8a, b, and c show the time series of area-mean water-vapor transport quantities in the CTL and sensitivity experiments from 0000 UTC 25 August to 1200 UTC 28 August 2015. The relative changes with respect to the CTL are shown in Figs. 8b, d, and f. Note that the relative change, $(r_s - r_0/r_0) \times 100\%$, is defined as the percentage of the quantity in sensitivity experiment (r_s) minus the quantity in the CTL (r_0), normalized by the quantity in the CTL (r_0).

Figure 8a shows the time series of area-averaged IWV. In the CTL, area-mean IWV decreases from 58 to 56 mm during the 84-h integration. When the low-level relative humidity is increased (decreased) by 10% in W10 (D10) experiment, the area-averaged IWV along the AR is increased (decreased) consistently. Since the IWV is not a function of horizontal wind speed, the mean IWVs in F10 and S10 runs are very similar. Note that the decrease of mean IWV implies the consumption of water vapor by condensation and deposition by convective processes. Figure 8b displays the time evolution of relative deviation of the IWV from sensitivity experiments with respect to the CTL. It reveals that the IWV is increased (decreased) by 5% when a 10% reduction in low-level (below 700 hPa) moisture is given initially in D10 experiment. The change of horizontal wind speed hardly influences the IWV.

Figure 8c shows the time series of area-mean IMT. When the moisture or wind speed is increased (decreased), the IMT is increased (decreased) as well. The mean IMT of almost all experiments (except for D10 experiment) increases with time after 12 hrs of model integration. Note that all

simulations underwent a spin-up process for the first 12 hrs because our model did not use any data assimilation. It is surprising that although the IMT is only a kinematic quantity, the mean IMT in W10 run has higher air mass transport than that in F10 run. Figure 8d shows the time series for the sensitivity of IMT among different experiments. It reveals that when 10% difference in horizontal wind speed below 700 hPa is given, the IMT is increased (or decreased) by less than 5%. On the other hand, when low-level moisture is increased (decreased) by 10%, the IMT can increase (or decrease) by 15%. Enhanced latent heat release may be responsible for the increase of IMT, but further study is required to understand the physical mechanism.

The IVT is the vertical integration of water-vapor flux which is a function of both water vapor and horizontal wind. The area-mean IVT is increased from 370 to 490 kg m^{-1} s^{-1} in the CTL experiment. The IVT is enhanced (reduced) in W10 and F10 (D10 and S10) experiments, as we expected (see Fig. 8e). Figure 8f shows the mean IVT is enhanced (reduced) by 20% in W10 (or D10) experiment, but enhanced (reduced) by less than 5% in F10 (S10) experiment. It seems that water-vapor transport is more sensitive to moisture than wind speed.

Since water-vapor transport is essential for the generation of precipitation, accumulated precipitation along the AR for all experiments is shown in Fig. 9a. It indicates that three rainfall events are captured in all simulations. The increasing trend of accumulated precipitation for low-level moisture enhancement experiment is more evident than that for wind-speed acceleration experiment. Likewise, the drying experiment (D10) has less accumulated precipitation than the wind-speed decreasing experiment (S10). In Fig. 9b, the time series of relative change of accumulated precipitation in W10 (D10) experiment is 20% (40%) more (less) than the
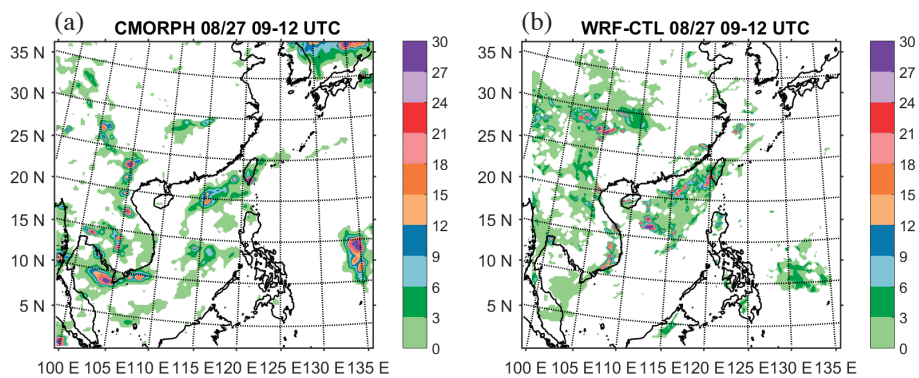

Fig. 4. The precipitation rate (unit: mm 3hr^{-1}) from the (a) CMORPH satellite precipitation data and (b) 27-km CTL simulation at 09 - 12 UTC 27 August 2015.
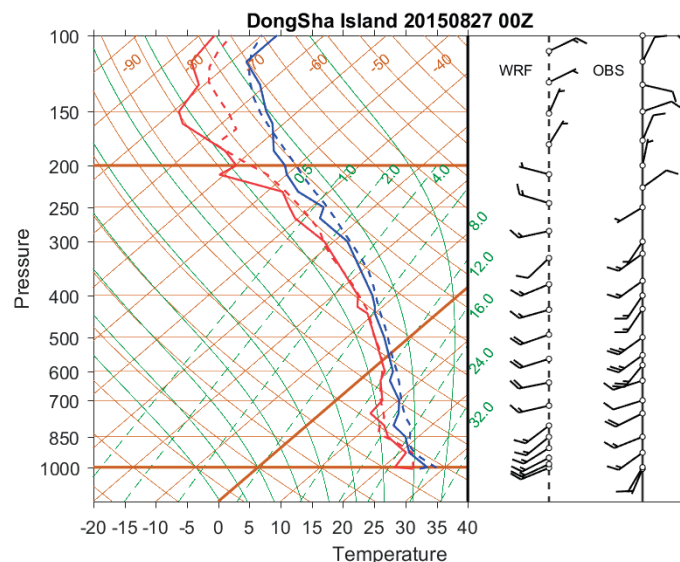

Fig. 5. Radiosonde observation (solid line) and WRF simulated data with 10 km radius averaging (dash line) at Dongsha Atoll at 27 August 2015. Red color indicates dew point temperature profile and blue color indicates temperature profile.
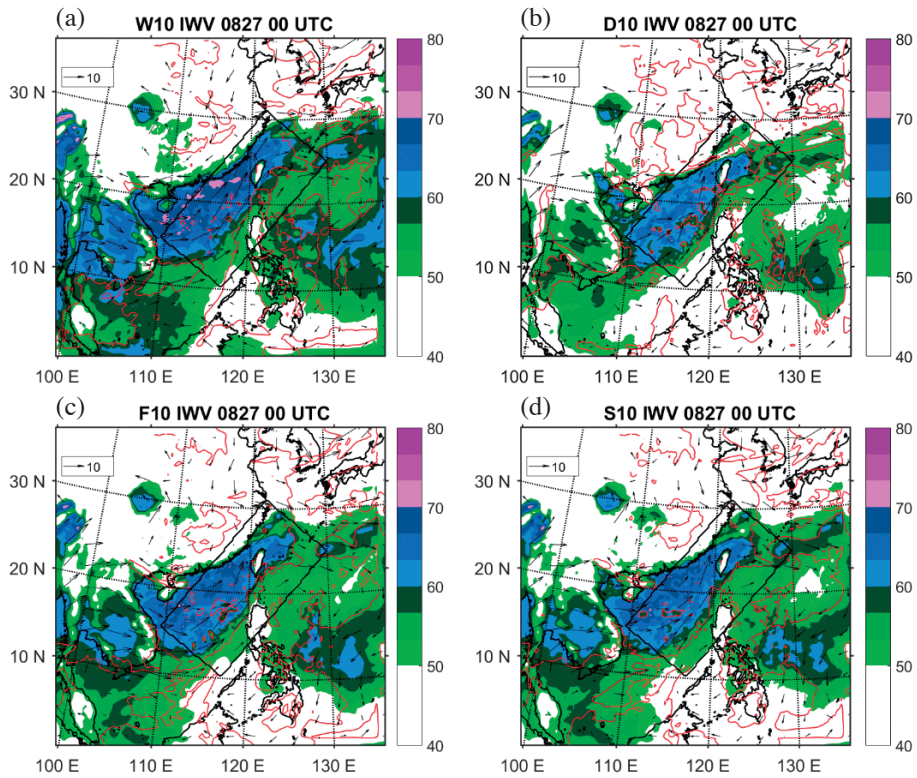
Fig. 6. The horizontal distribution of integrated water vapor (IWV; unit: mm) from the (a) W10, (b) D10, (c) F10, and (d) S10 experiments on 27-km gird. The red contours indicate the relative-humidity contours of 70% at 850 hPa and the vectors are horizontal wind vectors at 850 hPa.
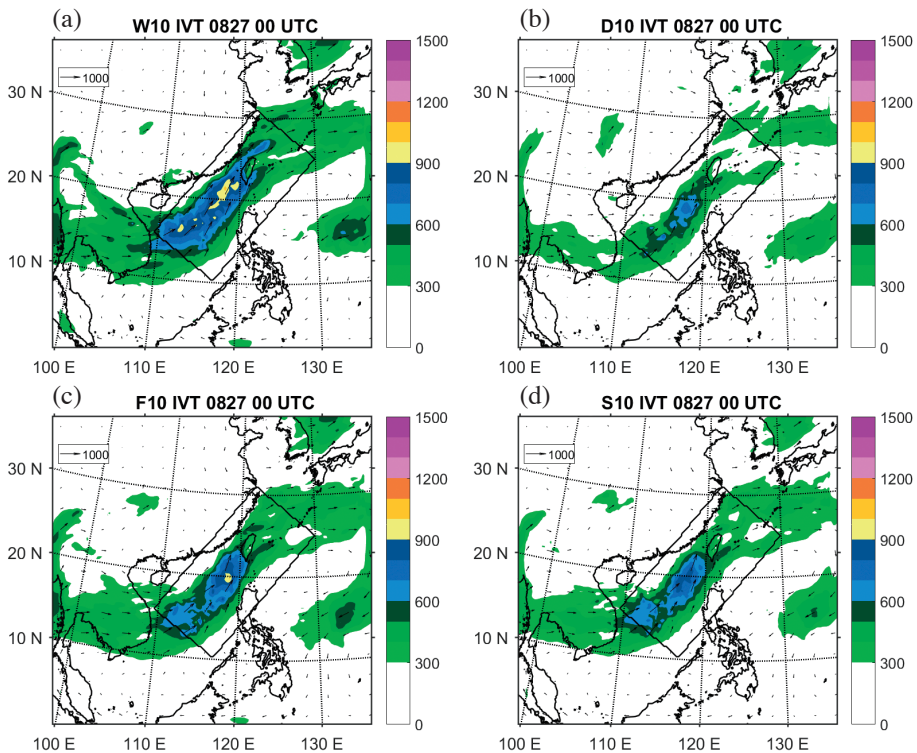

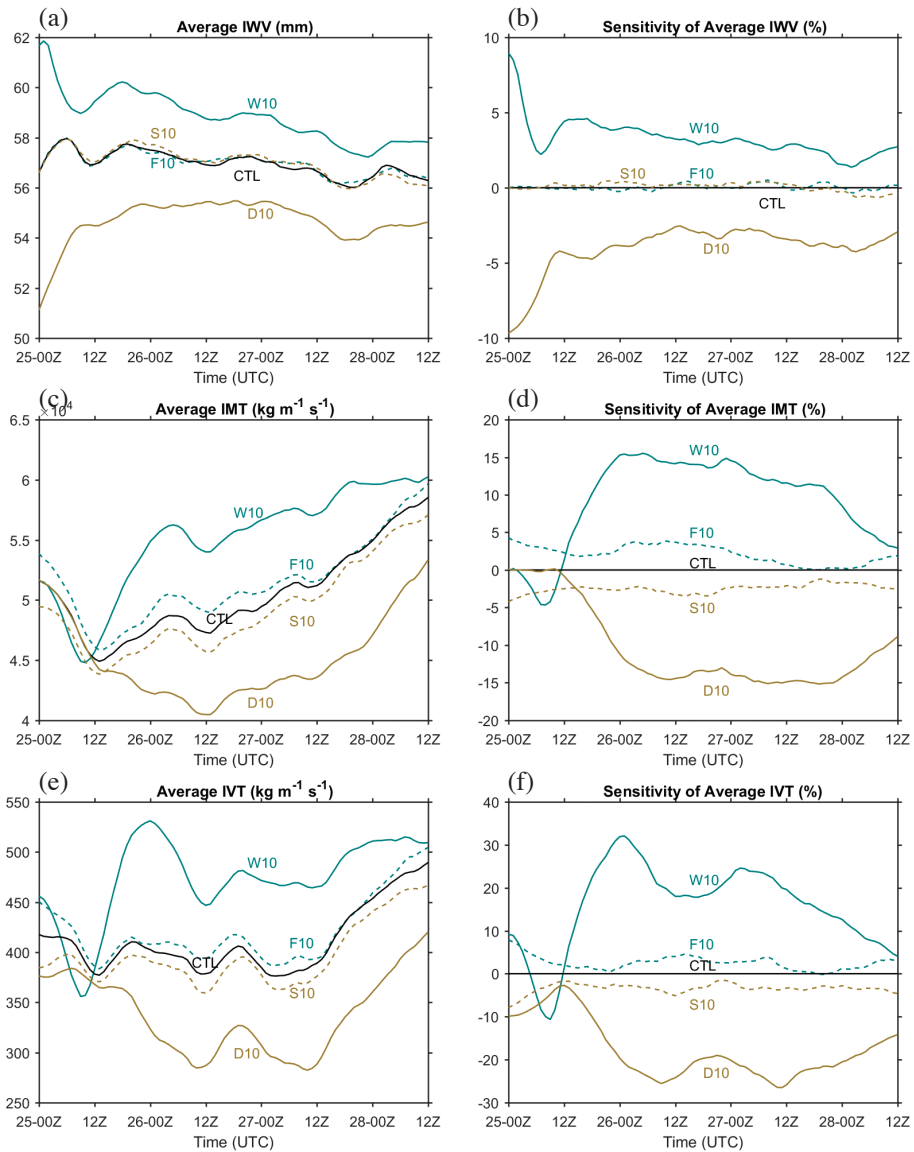Fig. 7. Similar to Fig. 6 but for integrated water-vapor transport (IVT; unit: kg m^{-1} s^{-1}).

Fig. 8. Time series of area-mean quantities for (a) integrated water vapor (IWV; unit: mm), (c) integrated mass transport (IMT; unit: kg m^{-1} s^{-1}), and (e) integrated water-vapor transport (IVT; unit: kg m^{-1} s^{-1}) averaged inside the slantwise rectangular box in CTL and sensitivity experiments. (b), (d), and (f) show the relative differences of area-mean IWV, IMT, and IVT between sensitivity experiments and CTL simulation, respectively.
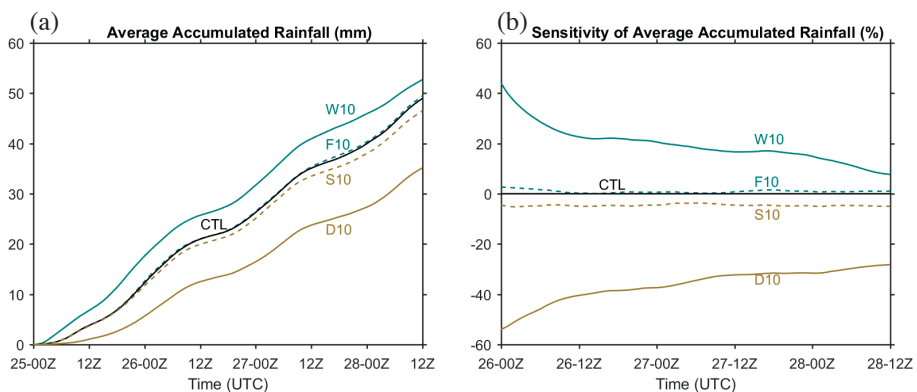

Fig. 9. Similar to Fig. 8 but for area-mean accumulated precipitation.

CTL. For wind-speed change experiments (F10 and S10), the relative accumulated-rainfall changes are less than 5%.

Horizontal water-vapor flux convergence [HFC; $-\nabla \cdot (q_v \overline{U})$] is considered as an important contributor to precipitation (Braun 2006; Yang et al. 2011; Huang et al. 2014). From vector analysis, the HFC can be decomposed into water-vapor advection (QADV; $-\overline{U} \cdot \nabla q_v$) and convergence [QCONV; $-q_v (\nabla \cdot \overline{U})$], that is,

$$-\nabla \cdot (q_v \overline{U}) = -\overline{U} \cdot \nabla q_v - q_v (\nabla \cdot \overline{U}) \tag{4a}$$

$$HFC = QADV + QCONV \tag{4b}$$

A time and volume integral of any quantity F is denoted as

$\{F\} = \int_{t_0}^{t} \int_V \rho F dV dt$. Figures 10a, b, and c show the evolution of {HFC}, {QADV}, and {QCONV} inside the slantwise box along the AR, respectively. The horizontal integral is for the slantwise box, the vertical integral is from surface to 200 hPa, and the time integral for 84 hrs with hourly data.

The positive slope periods in Fig. 10a correspond to the heavy rainfall events. While water vapor is increased at lower levels, more HFC is found within the slantwise box along the AR. As horizontal wind speed is either increased or decreased by 10%, the corresponding change of HFC is relatively week. Figures 10d, e, and f show the relative changes of {HFC}, {QADV}, and {QCONV} from sensitivity experiments with respect to the CTL experiment, respectively. The relative changes of {HFC}, {QADV}, and {QCONV} to the CTL in Figs. 10d, e, and f are qualitatively similar,
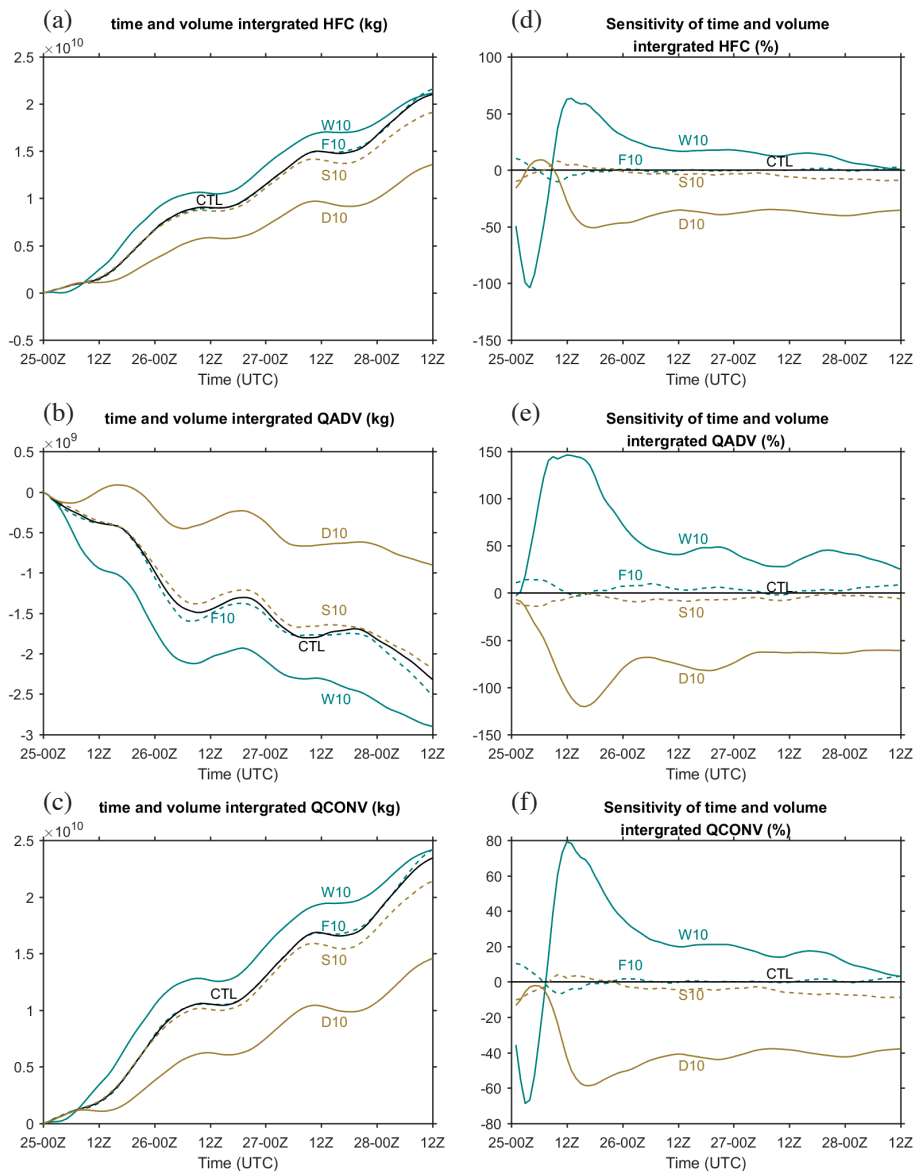

Fig. 10. Similar to Fig. 8 but for volume and time integrated (a) - (b) horizontal water vapor flux convergence {HFC}, (c) - (d) water vapor advection {QADV}, and (e) - (f) water vapor convergence {QCONV}.

although there are some small differences in magnitudes.

To better understand the relationship among {HFC}, {QADV}, and {QCONV}, we can rewrite Eq. (4) as follows:

$$\{HFC_S\} = \{QADV_S\} + \{QCONV_S\} \tag{5a}$$

$$\{HFC_C\} = \{QADV_C\} + \{QCONV_C\} \tag{5b}$$

where subscripts S indicates that the variables are from the sensitivity experiment, and subscript C indicates that variables are from the CTL. Subtracting Eq. (5a) from Eq. (5b) yield

$$\{\delta HFC_S\} = \{\delta QADV_S\} + \{\delta QCONV_S\} \tag{6}$$

where the symbol δ denotes the difference between sensitivity experiment and the CTL. Dividing Eq. (6) by {HFC$_C$} on both sides, the equation becomes

$$\frac{\{\delta HFC_S\}}{\{HFC_C\}} = C_1 \frac{\{\delta QADV_S\}}{\{QADV_C\}} + C_2 \frac{\{\delta QCONV_S\}}{\{QCONV_C\}} \tag{7a}$$

where

$$C_1 = \frac{\{\delta QADV_C\}}{\{HFC_C\}}, \quad C_2 = \frac{\{\delta QCONV_C\}}{\{HFC_C\}} \tag{7b}$$

Note that both coefficients C_1 and C_2 are determined by CTL simulation. Figure 11 shows the evolution of C_1 and C_2 along the AR. Coefficients C_1 and C_2 represent the contributions of water-vapor advection and wind convergence to the HFC in control run, respectively. The relative deviation parts (as shown in Figs. 9e and f), $\frac{\{\delta QADV_S\}}{\{QADV_C\}}$ and $\frac{\{\delta QCONV_S\}}{\{QCONV_C\}}$, represent the relative contributions by the sensitivity experiments (in the change of water vapor and wind speed) from the control run.

Figure 10 shows that QCONV is the main positive contributor to HFC, and QADV is the minor but negative contributor to HFC. This indicates that moisture is concentrated through wind convergence but water-vapor advection tends to reduce the moisture transport in this AR case. In moisture sensitivity experiments, the effects on HFC by QCONV and QADV are so significant that precipitation varies obviously. On the other hand, the wind-speed sensitivity experiments have little influence on QADV and QCONV, thus the HFC and precipitation have only minor differences.

Water vapor flux combines both horizontal wind vector and water vapor. It reveals that wind-speed change at low levels has limited impacts on water-vapor transport, HFC, and precipitation from large- or synoptic-scale perspectives. However, water-vapor change at low levels has significant impacts on water-vapor transport, HFC, and precipitation change.

4. CONVECTION IN MESOSCALE CONVECTIVE SYSTEMS

The MCS occurring from northern SCS to Taiwan from 1800 UTC 26 August to 1200 UTC 27 August 2015 is chosen to investigate the evolution of PE and other microphysics ratios. This MCS has an outstanding contribution in precipitation during its life cycle from large-scale perspective (Fig. 9a). A slantwise rectangular box of 420 km by 360 km is chosen to enclose the target MCS. This box follows the movement of the target MCS in a quasi-Lagranian framework.

Figure 12 shows the evolution of radar composite for the target MCS in CTL simulation. The MCS was initiated and developed to the northwest of Luzon Island (Fig. 12a). The system propagated northeastward within the southwesterly monsoon flow (Fig. 12b). Another line convection from southwestern China (Fujian) propagating southeastward combined with the target MCS (Fig. 12c). The MCS moved toward Taiwan, interacted with the CMR, and weakened afterwards (Fig. 12d).

In sensitivity experiments, the moistening run reveals a wider and stronger radar-echo structure (Fig. 13a), but the drying run displays a scattered and weaker feature (Fig. 13b). Increasing (decreasing) horizontal wind speed leads to a faster (slower) propagation speed, but the precipitation structure remains similar to that of the CTL (Figs. 13c and d).

Water budget can be decomposed into water-vapor and hydrometeor budgets. Following Braun (2006), Yang et al. (2011), and Huang et al. (2014), water-vapor and hydrometeor budget equations are written as:

$$\begin{aligned} Tend_v = {} & HFC_v + VFC_v + Div_v + PBL_v + Diff_v \\ & - Cond + Evap + Resd_v \end{aligned} \tag{8a}$$

$$\begin{aligned} Tend_h = {} & HFC_h + VFC_h + Div_h + PBL_h + Diff_h \\ & + Cond - Evap - P + Resd_h \end{aligned} \tag{8b}$$

where subscripts v and h indicate the terms related to water vapor and hydrometeor, Tend is the tendency term, HFC is the horizontal flux convergence term, VFC is the vertical flux convergence term, Div is the three dimensional divergence term, PBL is the planetary boundary layer term, Diff is the diffusion term, Cond is the total condensation, Evap is the total evaporation, P is the precipitation flux, and Resd is the residual term. Total condensation (Cond) includes both condensation and deposition, and total evaporation (Evap) includes both evaporation and sublimation. Precipitation flux is outputted from the sedimentation term in Morrison scheme.

Most terms in Eq. (8) are directly calculated from WRF

outputs except that tendency terms are calculated by central finite-difference scheme using model outputs at 5-min intervals. Residual terms are obtained by subtracting the tendency from the summation of other terms on the right-hand side in Eqs. (8a) and (8b). Note that residual terms include the truncation errors from temporal difference, redistribution of the negative hydrometeor mass from spatial differencing, and truncation errors in spatial finite differencing. Thus, residual terms should be small enough to have a reasonable accuracy of budget calculation.

All budget terms are calculated in a storm-following framework, in which the storm position is updated every 5 min. The budget terms are first integrated vertically, and then the area integration is conducted within the box enclosing the storm. These budget terms are calculated from 1800 UTC 26 August to 1200 UTC 27 August 2015 for 18 hrs and the results are shown in Figs. 14 and 15.

Table 1 shows the water-vapor and hydrometeor budgets after temporal and volumetric integration for the CTL and sensitivity experiments. The second row shows the mass of total condensation (Cond) for each experiment. The rest of rows show the water-budget terms normalized by total condensation in each experiment. It can be seen that Cond, Evap, HFC, and PBL are the main contributors in vapor budget, and Cond, Evap, and P are dominated in hydrometeor budget. Residual terms (Resd) are less than ±3%, indicating that the budget calculations are reliable (see also Figs. 14 and 15). Similarly, total condensation (Cond) increases (decreases) when low-level water vapor is increased (decreased) in W10 (D10) experiment. Furthermore, as wind speed at low levels is increased (decreasd) in F10 (S10) experiment, Cond is only increased (decreased) slightly. For vapor budget, Evap, HFC, and P are approximately 40 - 50% of Cond and PBL_v is only 10% of Cond.

Figures 14 and 15 show the evolution of major components of the volume integral of water-vapor and hydrometeor budget terms, respectively. Water vapor from the environment supplies the Cond through HFC_v and eventually converts into precipitation. For the CTL, the time series reveals that the peak of HFC_v (in Fig. 14a) occur at 04 UTC, slightly earlier than the peaks of Cond (in Figs. 14a and 15a) and precipitation (P in Fig. 15a) at 05 UTC, because hydrometeors need some time to condensate and fall down. All Cond, HFC_v and P have clear enhanced signals in the time series when water vapor or horizontal wind speed is increased at lower levels (W10 and F10 experiments). The increase of water vapor and horizontal wind speed may promote the production rates of HFC_v, Cond and P, but the signals are not remarkable in experiment F10. Note that PBL_v decreases with time, as a result of the inland propagation of the MCS (Fig. 14).

The PE can be defined from macroscopic or microscopic prospectives. According to Sui et al. (2007), large-scale precipitation efficiency (LSPE) and cloud-microphysics precipitation efficiency (CMPE) can be defined as:

$$LSPE = \frac{P}{\sum_{i=1}^{4} H(Q_i) Q_i} \tag{9}$$

$$CMPE = \frac{P}{Cond + H(Q_{CM}) Q_{CM}} \tag{10}$$

where $Q_i = (Q_{WVT}, Q_{WVF}, Q_{WVE}, Q_{CM})$, H is the Heaviside function in which $H(F) = 1$ when $F > 0$, and $H(F) = 0$ when $F \leq 0$. Q_{WVT} is the local change of water vapor, Q_{WVF} is HFC_v, Q_{WVE} is the surface evaporation, and Q_{CM} is the local change of hydrometeors and HFC_h. The PE is an important parameter in cumulus parameterization and highly related to precipitation mechanism.

In addition to the PE, three other microphysics ratios are proposed by Huang et al. (2014), including the condensation ratio (CR), deposition ratio (DR), and raindrop evaporation ratio (ER). These three ratios are defined as follow:
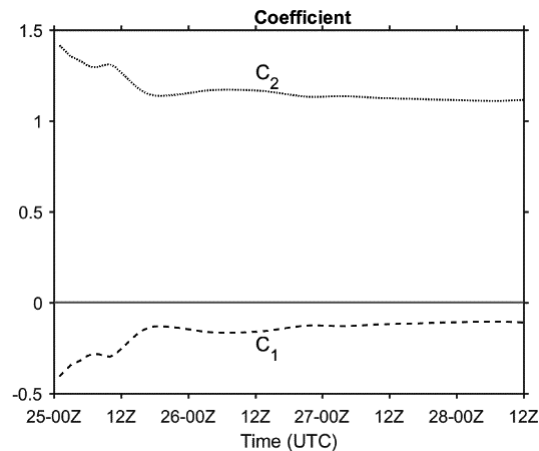

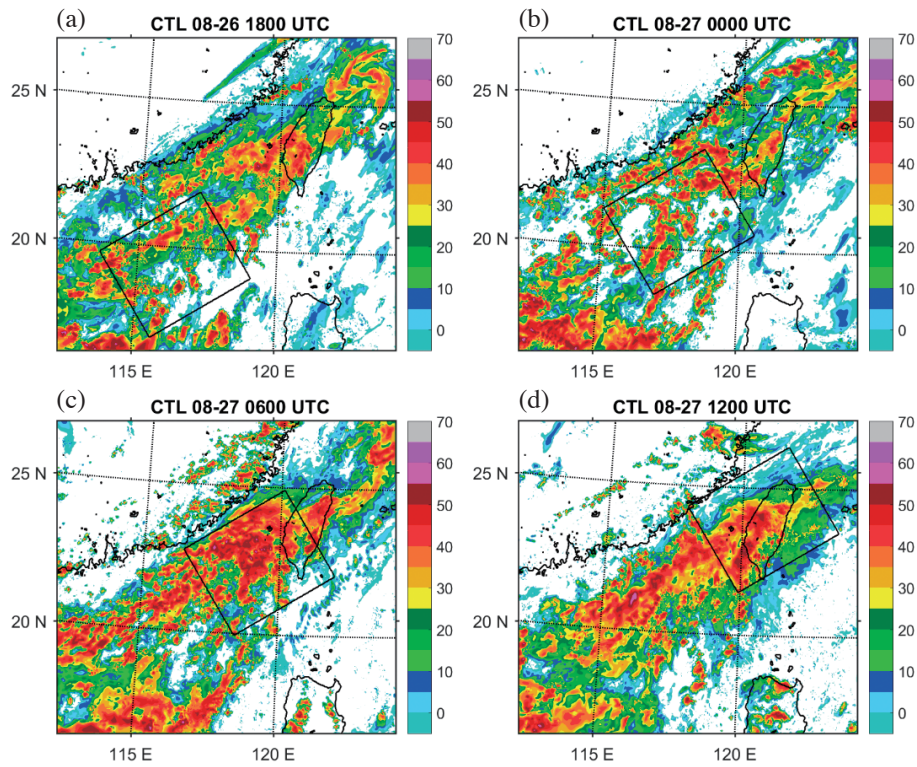Fig. 11. Time series of coefficients C_1 and C_2 in Eq. (7).

Fig. 12. The horizontal distribution of radar reflectivity composite in 3-km CTL simulation at (a) 1800 UTC 26 August, (b) 0000 UTC, (c) 0600 UTC, and (d) 1200 UTC 27 August 2015. The slantwise rectangular box shows the MCS location.
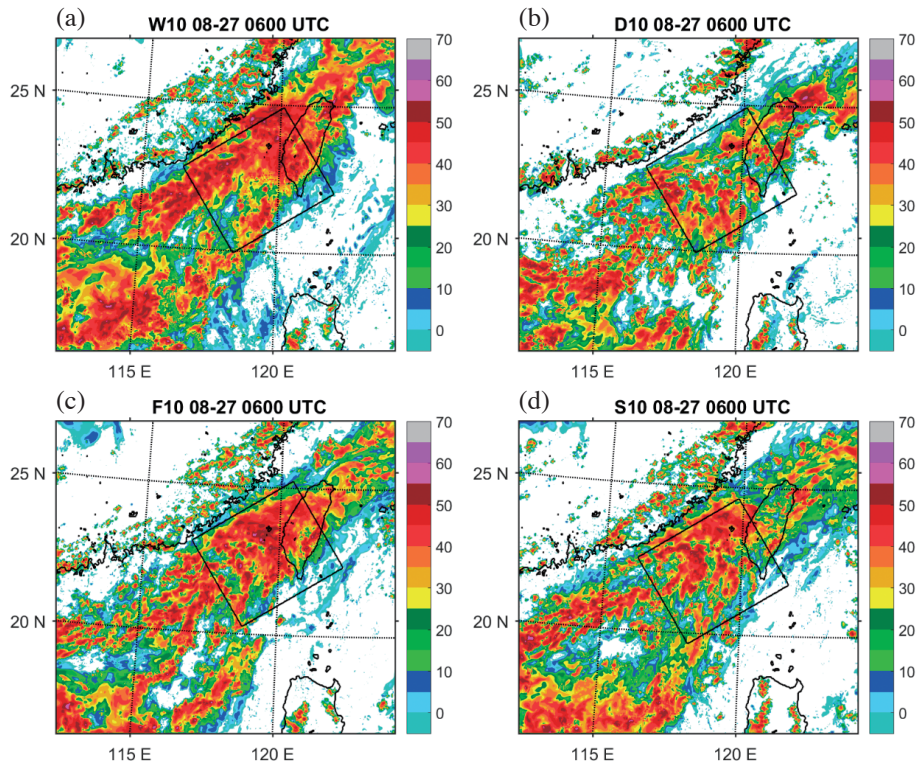

Fig. 13. Similar to Fig. 12 but for the (a) W10, (b) D10, (c) F10, and (d) S10 experiments at 0600 UTC 27 August 2015.

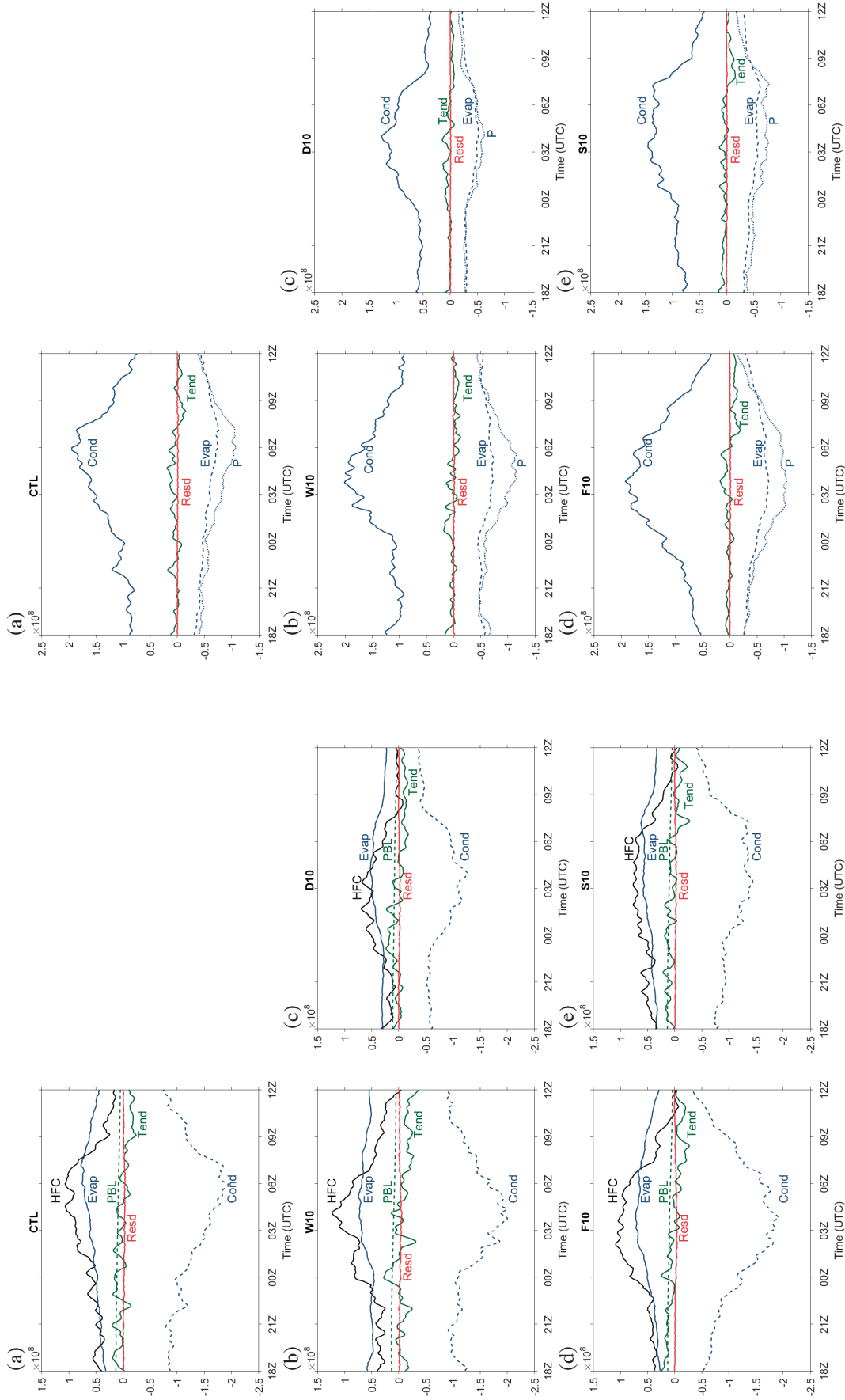Fig. 15. Similar to Fig. 14 but for hydrometeor budget.

Fig. 14. Time series of major components in water-vapor budget within the MCS-following box for the (a) CTL, (b) W10, (c) D10, (d) F10, and (e) S10 experiments.

Table 1. The volume- and time-integrated water budget, including the water-vapor (WV) and hydrometeors (HY) budgets, are summarized in this table. The second row shows the total mass of condensation, including condensation and deposition, inside the rectangular box. All budget terms are normalized by total condensation.

	CTL		W10		D10		F10		S10	
Cond (10^{12} kg)	8.09		8.57		4.69		7.68		6.49	
	WV	HY	WV	HY	WV	HY	WV	HY	WV	HY
Cond	-100.00	100.00	-100.00	100.00	-100.00	100.00	-100.00	100.00	-100.00	100.00
Evap	43.76	-43.76	43.96	-43.96	49.53	-49.53	43.08	-43.08	45.44	-45.44
HFC	48.30	0.05	42.63	0.03	37.68	1.10	50.55	-0.15	47.19	0.09
VFC	0.01	0.00	0.01	0.00	0.01	0.00	0.01	0.00	0.01	0.00
Div	1.90	0.43	1.76	0.35	1.49	0.43	1.89	0.39	1.73	0.41
Diff	0.00	-0.01	0.00	0.00	-0.01	-0.01	0.00	0.00	0.00	0.01
PBL	7.44	0.00	7.25	0.00	10.81	0.00	8.41	0.00	9.62	0.00
Tend	-0.41	1.92	-6.27	0.53	-1.78	1.15	2.14	1.68	2.40	1.43
Resd	-1.82	-2.50	-1.88	-0.99	-1.29	-1.81	-1.80	-2.15	-1.59	-1.97
P		-54.21		-55.43		-50.18		-55.01		-53.10

$$CR = \frac{Cond_l}{Cond + H(Q_{CM})Q_{CM}} \qquad (11)$$

$$DR = \frac{Cond_s}{Cond + H(Q_{CM})Q_{CM}} \qquad (12)$$

$$ER = \frac{Evap_r}{Cond + H(Q_{CM})Q_{CM}} \qquad (13)$$

where $Cond_l$ is liquid-phase condensation rate, $Cond_s$ is ice-phase deposition rate, and $Evap_r$ is raindrop evaporation rate.

Figure 16 shows the time series of PEs, rainfall rate, and microphysics ratios in the quasi-Lagrangian framework following the propagation of targeted MCS from the SCS to Taiwan. Shading area in Fig. 16 represents the top 30% topography height in the moving rectangular box. PEs increase (with the CMPE of 30 - 40% and the LSPE of 10 - 20%) when the MCS approaches Taiwan terrain. Furthermore, CMPE is larger than LSPE, suggesting that not all moisture transported into the MCS through HFC_v can be converted into condensation and deposition. The maximum of rainfall rate occurs at or slightly after the landfall of MCS on Taiwan. CR reaches 60% at the developing stage (18 - 21 UTC 26 August) and decreases to 40% at the decaying stage (06 - 12 UTC 27 August). DR steadily stays around 10 - 15% at the developing stage, and reaches 40% at the decaying stage. ER increases after the increase of rainfall rate and reaches 10 - 20%. DR increases as the MCS moves over the Taiwan topography, indicating ice-phase microphysical processes become more important at later (decaying) stage of the MCS.

PEs and microphysics ratios do not have remarkable differences in four sensitivity experiments, compared to those in the CTL. It is found that the rainfall is mainly dominated by Cond, because plenty of water vapor was available at low levels along the southwesterly monsoon flow. Note that the peak PE over the terrain for the MCS embedded in the southwesterly monsoon flow is less than those (~100%) found in deep convective cells or rainbands in landfalling typhoons (Huang et al. 2014; Xu et al. 2017), and a larger average box and a weaker convective system in this study may account for the difference.

5. CONCLUSIONS

In this study, a triply-nested WRF model is used to simulate an atmospheric river event associated with the southwesterly monsoon flow over the SCS and Taiwan on 25 - 28 August 2015. The southwesterly flow transports abundant moisture from the Bay of Bengal, the Indochina, the SCS, and Taiwan. The warm sea surface temperature over the SCS supplies plenty of water vapor. Torrential rainfall occurs in the southwestern Taiwan during the inland penetration of moisture along the southwesterly flow. In addition to the CTL simulation, four sensitivity experiments are conducted to investigate the evolution of large-scale moisture transport, PE, and other microphysics ratios given a change of relative humidity by ±10% and horizontal wind speed by ±10% at low levels (below 700 hPa).

Large-scale water vapor transports indicated by the IWV, IMT, and IVT within the southwesterly flow are calculated inside a slantwise rectangular box of 2025 × 945 km^2 on the outermost 27-km grid. We found that changing the low-level relative humidity by ±10% would increase/decrease the IWV by 5%, the IMT by 15%, and the IVT by 20%. On the other hand, if the horizontal wind speed is changed by ±10%, the IWV will not change obviously, and the IMT and
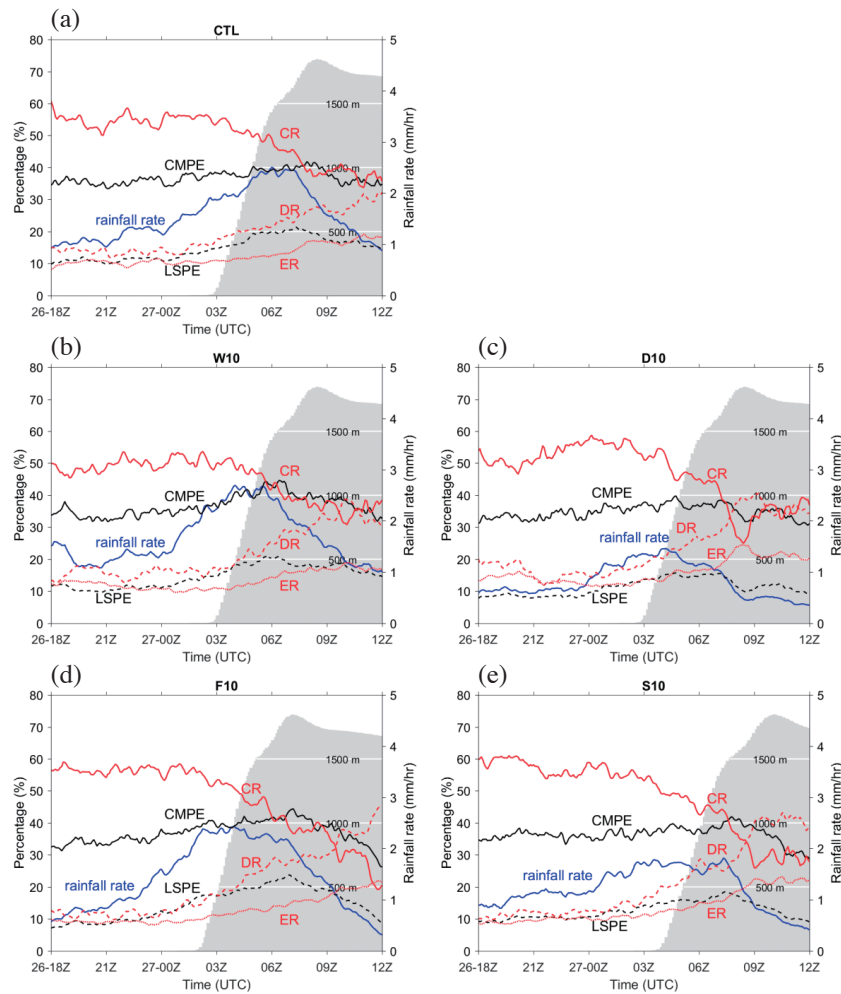
Fig. 16. Time series of cloud-microphysics precipitation efficiency (CMPE; black line), large-scale precipitation efficiency (LSPE; black dash line), rainfall rate (blue line), condensation ratio (CR; red line), deposition ratio (DR; red dash line), and raindrop evaporation ratio (ER; red dot line) averaged inside the MCS-following box for the (a) CTL, (b) W10, (c) D10, (d) F10, and (e) S10 experiments. Shaded areas are the top 30% terrain height within the box.

IVT will increase/decrease by 5%. The increase of low-level moisture not only enhances the amount of water vapor content, but also provides stronger and deeper convection to intensify the IMT. However, the increase of horizontal wind speed only increases the IMT slightly, and the IWV almost remains consistent. Although horizontal water-vapor flux is the multiple of water-vapor mixing ratio by horizontal wind vector, the IVT in the moistening experiment changes more significantly than the wind-speed accelerating experiment.

Sensitivity experiments show that the accumulated rainfall along the southwesterly flow can have 20% enhancement (40% reduction) in moistening or W10 (drying or D10) experiment, while the wind-speed sensitivity experiments have less change on accumulated rainfall (Table 2). Water vapor provided by wind convergence (QCONV) is the major contributor to water-vapor flux convergence (HFC), and water vapor advection (QADV) is the minor but negative contributor to HFC.

In the moistening and wind-accelerating scenarios, the MCS convection would become stronger and more clustering pattern along the southwesterly monsoon flow. In contrast, weaker and scattering convection appear in the drying and wind-decelerating scenarios (see the conceptual model in Fig. 17). A slantwise rectangular box of 420 km by 360 km is chosen to follow the movement of the MCS. Water budget, PE, and microphysics ratios are calculated in the quasi-Lagrangian framework. Budget analyses are reliable in control and four sensitivity experiments because the residual terms are relatively small (only up to 3% of the largest budget terms). Each normalized budget term is similar in all experiments, and the vapor and hydrometeor budgets are more (less) sensitive to low-level relative humidity (wind speed). Microphysical ratios of CR, DR, and ER show small differences in sensitivity experiments. When the MCS approaches the CMR on Taiwan, the LSPE increases from 10 to 20%, the CMPE increases from 30 to 40%, and the DR

Table 2. The change of IWV, IMT, IVT, HFC, and P in sensitivity experiments with respect to the CTL.

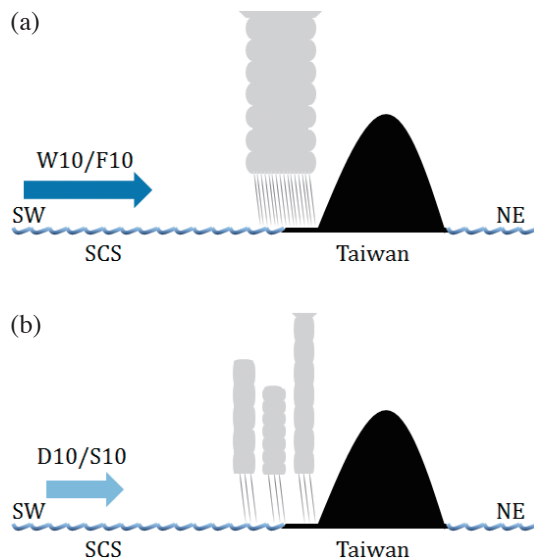| Exp.	IWV	IMT	IVT	HFC	P
W10	5%	15%	20%	15%	20%
F10	~0%	5%	5%	< 1%	< 5%
S10	~0%	-5%	-5%	-5%	-5%
D10	-5%	-15%	-20%	-40%	-40%

Fig. 17. Conceptual model of water-vapor transport, clouds, and precipitation developing in different environmental conditions for (a) W10/F10 and (b) S10/D10 experiments within the southwesterly monsoon flow.

increases from 10 to 40%; all indicate more production of surface rainfall and more importance of ice-phase microphysical processes over the CMR.

Finally, conclusions obtained in this study are mainly based on numerical simulations with some model deficiencies, physics uncertainties, and numerical errors, thus we should keep these caveats in mind. In particular, our modeling study uses only one type of microphysics scheme (Morrison) to simulate the evolution of water budget and precipitation efficiency of the MCS embedded in the southwesterly monsoon flow over the SCS, other microphysics schemes should be tested in the future to confirm whether our results depend on a specific microphysics parameterization or not. More MCS cases along atmospheric rivers in this region (Chen et al. 2020; Sui et al. 2020; Tu et al. 2020) or other geographic locations (for example, west coast of the U.S.A.) or under different synoptic settings should be investigated in the future to generalize the conclusions obtained from this case study.

REFERENCES

Bao, J.-W., S. A. Michelson, P. J. Neiman, F. M. Ralph, and J. M. Wilczak, 2006: Interpretation of enhanced integrated water vapor bands associated with extratropical cyclones: Their formation and connection to tropical moisture. *Mon. Weather Rev.*, **134**, 1063-1080, doi: 10.1175/MWR3123.1. [Link]

Brands, S., J. M. Gutiérrez, and D. San-Martín, 2017: Twentieth-century atmospheric river activity along the west coasts of Europe and North America: Algorithm formulation, reanalysis uncertainty and links to atmospheric circulation patterns. *Climate Dyn.*, **48**, 2771-2795, doi: 10.1007/s00382-016-3095-6. [Link]

Braun, S. A., 2006: High-resolution simulation of Hurricane Bonnie (1998). Part II: Water budget. *J. Atmos. Sci.*, **63**, 43-64, doi: 10.1175/JAS3609.1. [Link]

Chen, C.-S. and Y.-L. Chen, 2003: The rainfall characteristics of Taiwan. *Mon. Weather Rev.*, **131**, 1323-1341, doi: 10.1175/1520-0493(2003)131<1323:TRCOT>2.0.CO;2. [Link]

Chen, J.-M., C.-H. Tsou, R. Wu, and C.-H. Sui, 2020: Introduction to the special issue on South China Sea Two-Island Monsoon Experiment (SCSTIMX): Observation, simulation, and projection. *Terr. Atmos. Ocean. Sci.*, **31**, 97-101, doi: 10.3319/TAO.2020.03.19.01. [Link]

Davis, C. A., 1992: Piecewise potential vorticity inversion. *J. Atmos. Sci.*, **49**, 1397-1411, doi: 10.1175/1520-0469(1992)049<1397:PPVI>2.0.CO;2. [Link]

Dee, D. P., S. M. Uppala, A. J. Simmons, P. Berrisford, P. Poli, S. Kobayashi, U. Andrae, M. A. Balmaseda, G. Balsamo, P. Bauer, P. Bechtold, A. C. M. Beljaars, L. van de Berg, J. Bidlot, N. Bormann, C. Delsol, R. Dragani, M. Fuentes, A. J. Geer, L. Haimberger, S. B. Healy, H. Hersbach, E. V. Hólm, L. Isaksen, P. Kållberg, M. Köhler, M. Matricardi, A. P. McNally, B. M. Monge-Sanz, J.-J. Morcrette, B.-K. Park, C. Peubey, P. de Rosnay, C. Tavolato, J.-N. Thépaut, and F. Vitart, 2011: The ERA-Interim reanalysis: Configuration and performance of the data assimilation system. *Q. J. R. Meteorol. Soc.*, **137**, 553-597, doi: 10.1002/qj.828. [Link]

Dettinger, M. D., F. M. Ralph, T. Das, P. J. Neiman, and

D. R. Cayan, 2011: Atmospheric rivers, floods and the water resources of California. *Water*, **3**, 445-478, doi: 10.3390/w3020445. [Link]

Du, Y. and G. Chen, 2019: Heavy rainfall associated with double low-level jets over southern China. Part II: Convection initiation. *Mon. Weather Rev.*, **147**, 543-565, doi: 10.1175/mwr-d-18-0102.1. [Link]

Dudhia, J., 1989: Numerical study of convection observed during the Winter Monsoon Experiment using a mesoscale two-dimensional model. *J. Atmos. Sci.*, **46**, 3077-3107, doi: 10.1175/1520-0469(1989)046<3077:NSOCOD>2.0.CO;2. [Link]

Gimeno, L., R. Nieto, M. Vázquez, and D. A. Lavers, 2014: Atmospheric rivers: A mini-review. *Front. Earth Sci.*, **2**, 2, doi: 10.3389/feart.2014.00002. [Link]

Grell, G. A. and D. Dévényi, 2002: A generalized approach to parameterizing convection combining ensemble and data assimilation techniques. *Geophys. Res. Lett.*, **29**, 38-1-38-4, doi: 10.1029/2002GL015311. [Link]

Hong, S.-Y., Y. Noh, and J. Dudhia, 2006: A new vertical diffusion package with an explicit treatment of entrainment processes. *Mon. Weather Rev.*, **134**, 2318-2341, doi: 10.1175/MWR3199.1. [Link]

Huang, H.-L., M.-J. Yang, and C.-H. Sui, 2014: Water budget and precipitation efficiency of Typhoon Morakot (2009). *J. Atmos. Sci.*, **71**, 112-129, doi: 10.1175/JAS-D-13-053.1. [Link]

Kamae, Y., W. Mei, S.-P. Xie, M. Naoi, and H. Ueda, 2017: Atmospheric rivers over the Northwestern Pacific: Climatology and interannual variability. *J. Clim.*, **30**, 5605-5619, doi: 10.1175/JCLI-D-16-0875.1. [Link]

Kuo, H. L., 1965: On formation and intensification of tropical cyclones through latent heat release by cumulus convection. *J. Atmos. Sci.*, **22**, 40-63, doi: 10.1175/1520-0469(1965)022<0040:OFAIOT>2.0.CO;2. [Link]

Kuo, H. L., 1974: Further studies of the parameterization of the influence of cumulus convection on large-scale flow. *J. Atmos. Sci.*, **31**, 1232-1240, doi: 10.1175/1520-0469(1974)031<1232:FSOTPO>2.0.CO;2. [Link]

Lavers, D. A., G. Villarini, R. P. Allan, E. F. Wood, and A. J. Wade, 2012: The detection of atmospheric rivers in atmospheric reanalyses and their links to British winter floods and the large-scale climatic circulation. *J. Geophys. Res.*, **117**, D20106, doi: 10.1029/2012JD018027. [Link]

Li, X., C.-H. Sui, and K.-M. Lau, 2002: Precipitation efficiency in the tropical deep convective regime: A 2-D cloud resolving modeling study. *J. Meteorol. Soc. Jpn.*, **80**, 205-212, doi: 10.2151/jmsj.80.205. [Link]

Lipps, F. B. and R. S. Hemler, 1986: Numerical simulation of deep tropical convection associated with large-scale convergence. *J. Atmos. Sci.*, **43**, 1796-1816, doi:

10.1175/1520-0469(1986)043<1796:NSODTC>2.0.CO;2. [Link]

Mlawer, E. J., S. J. Taubman, P. D. Brown, M. J. Iacono, and S. A. Clough, 1997: Radiative transfer for inhomogeneous atmospheres: RRTM, a validated correlated-k model for the longwave. *J. Geophys. Res.*, **102**, 16663-16682, doi: 10.1029/97JD00237. [Link]

Morales, A., H. Morrison, and D. J. Posselt, 2018: Orographic precipitation response to microphysical parameter perturbations for idealized moist nearly neutral flow. *J. Atmos. Sci.*, **75**, 1933-1953, doi: 10.1175/JAS-D-17-0389.1. [Link]

Morrison, H. and A. Gettelman, 2008: A new two-moment bulk stratiform cloud microphysics scheme in the Community Atmosphere Model, Version 3 (CAM3). Part I: Description and numerical tests. *J. Clim.*, **21**, 3642-3659, doi: 10.1175/2008JCLI2105.1. [Link]

Morrison, H., G. Thompson, and V. Tatarskii, 2009: Impact of cloud microphysics on the development of trailing stratiform precipitation in a simulated squall line: Comparison of one- and two-moment schemes. *Mon. Weather Rev.*, **137**, 991-1007, doi: 10.1175/2008MWR2556.1. [Link]

Mueller, M. J., K. M. Mahoney, and M. Hughes, 2017: High-resolution model-based investigation of moisture transport into the Pacific Northwest during a strong atmospheric river event. *Mon. Weather Rev.*, **145**, 3861-3879, doi: 10.1175/MWR-D-16-0466.1. [Link]

Neiman, P. J., F. M. Ralph, G. A. Wick, J. D. Lundquist, and M. D. Dettinger, 2008a: Meteorological characteristics and overland precipitation impacts of atmospheric rivers affecting the west coast of North America based on eight years of SSM/I satellite observations. *J. Hydrometeorol.*, **9**, 22-47, doi: 10.1175/2007JHM855.1. [Link]

Neiman, P. J., F. M. Ralph, G. A. Wick, Y.-H. Kuo, T.-K. Wee, Z. Ma, G. H. Taylor, and M. D. Dettinger, 2008b: Diagnosis of an intense atmospheric river impacting the Pacific Northwest: Storm summary and offshore vertical structure observed with COSMIC satellite retrievals. *Mon. Weather Rev.*, **136**, 4398-4420, doi: 10.1175/2008MWR2550.1. [Link]

Ralph, F. M., P. J. Neiman, and G. A. Wick, 2004: Satellite and CALJET aircraft observations of atmospheric rivers over the eastern North Pacific ocean during the winter of 1997/98. *Mon. Weather Rev.*, **132**, 1721-1745, doi: 10.1175/1520-0493(2004)132<1721:SACAOO>2.0.CO;2. [Link]

Ralph, F. M., P. J. Neiman, and R. Rotunno, 2005: Dropsonde Observations in Low-Level Jets over the Northeastern Pacific Ocean from CALJET-1998 and PACJET-2001: Mean vertical-profile and atmospheric-river characteristics. *Mon. Weather Rev.*, **133**, 889-910, doi: 10.1175/MWR2896.1. [Link]

Ramos, A. M., R. M. Trigo, M. L. R. Liberato, and R. Tomé, 2015: Daily precipitation extreme events in the Iberian Peninsula and its association with atmospheric rivers. *J. Hydrometeorol.*, **16**, 579-597, doi: 10.1175/ JHM-D-14-0103.1. [Link]

Schumacher, R. S., 2015: Sensitivity of precipitation accumulation in elevated convective systems to small changes in low-level moisture. *J. Atmos. Sci.*, **72**, 2507-2524, doi: 10.1175/JAS-D-14-0389.1. [Link]

Skamarock, W. C., J. B. Klemp, J. Dudhia, D. O. Gill, D. M. Barker, M. G. Duda, X.-Y. Huang, W. Wang, and J. G. Powers, 2008: A Description of the Advanced Research WRF Version 3, NCAR Technical Note, No. NCAR/TN-475+STR, University Corporation for Atmospheric Research, National Center for Atmospheric Research, Boulder, Colorado, USA, 113 pp, doi: 10.5065/D68S4MVH. [Link]

Smith, B. L., S. E. Yuter, P. J. Neiman, and D. E. Kingsmill, 2010: Water vapor fluxes and orographic precipitation over Northern California associated with a landfalling atmospheric river. *Mon. Weather Rev.*, **138**, 74-100, doi: 10.1175/2009MWR2939.1. [Link]

Stohl, A., C. Forster, and H. Sodemann, 2008: Remote sources of water vapor forming precipitation on the Norwegian west coast at 60°N—A tale of hurricanes and an atmospheric river. *J. Geophys. Res.*, **113**, D05102, doi: 10.1029/2007JD009006. [Link]

Sui, C.-H., X. Li, and M.-J. Yang, 2007: On the definition of precipitation efficiency. *J. Atmos. Sci.*, **64**, 4506-4513, doi: 10.1175/2007jas2332.1. [Link]

Sui, C.-H., P.-H. Lin, W.-T. Chen, S. Jan, C.-Y. Liu, Y.-J. Yang, C.-H. Liu, J.-M. Chen, M.-J. Yang, J.-S. Hong, L.-H. Hsu, and L.-S. Tseng, 2020: The South China Sea Two Islands Monsoon Experiment for studying convection and subseasonal to seasonal variability. *Terr. Atmos. Ocean. Sci.*, **31**, 103-129, doi: 10.3319/ TAO.2019.11.29.02. [Link]

Teng, J.-H., C.-S. Chen, T.-C. C. Wang, and Y.-L. Chen, 2000: Orographic effects on a squall line system over Taiwan. *Mon. Weather Rev.*, **128**, 1123-1138, doi:

10.1175/1520-0493(2000)128<1123:OEOASL>2.0. CO;2. [Link]

Tu, C.-C., Y.-L. Chen, P.-L. Lin, and Y. Du, 2019: Characteristics of the marine boundary layer jet over the South China Sea during the early summer rainy season of Taiwan. *Mon. Weather Rev.*, **147**, 457-475, doi: 10.1175/mwr-d-18-0230.1. [Link]

Tu, C.-C., Y.-L. Chen, P.-L. Lin, and P.-H. Lin, 2020: The relationship between the boundary layer moisture transport from the South China Sea and heavy rainfall over Taiwan. *Terr. Atmos. Ocean. Sci.*, **31**, 159-176, doi: 10.3319/TAO.2019.07.01.01. [Link]

Weisman, M. L. and J. B. Klemp, 1982: The dependence of numerically simulated convective storms on vertical wind shear and buoyancy. *Mon. Weather Rev.*, **110**, 504-520, doi: 10.1175/1520-0493(1982)110<0504:TD ONSC>2.0.CO;2. [Link]

Xu, H., G. Zhai, and X. Li, 2017: Precipitation efficiency and water budget of Typhoon Fitow (2013): A particle trajectory study. *J. Hydrometeorol.*, **18**, 2331-2354, doi: 10.1175/JHM-D-16-0273.1. [Link]

Yang, M.-J., S. A. Braun, and D.-S. Chen, 2011: Water budget of Typhoon Nari (2001). *Mon. Weather Rev.*, **139**, 3809-3828, doi: 10.1175/MWR-D-10-05090.1. [Link]

Yeh, H.-C. and Y.-L. Chen, 1998: Characteristics of rainfall distributions over Taiwan during the Taiwan Area Mesoscale Experiment (TAMEX). *J. Appl. Meteorol.*, **37**, 1457-1469, doi: 10.1175/1520-0450(1998)037<1457:CORDOT>2.0. CO;2. [Link]

Yeh, H.-C. and Y.-L. Chen, 2002: The role of offshore convergence on coastal rainfall during TAMEX IOP 3. *Mon. Weather Rev.*, **130**, 2709-2730, doi: 10.1175/1520-0493(2002)130<2709:TROOCO>2.0. CO;2. [Link]

Zhu, Y. and R. E. Newell, 1998: A proposed algorithm for moisture fluxes from atmospheric rivers. *Mon. Weather Rev.*, **126**, 725-735, doi: 10.1175/1520-0493(1998)126<0725:APAFMF>2.0. CO;2. [Link]